BaHfO$_3$ artificial pinning centres in TFA-MOD-derived YBCO and GdBCO thin films

M Erbe[1,2]**, J Hänisch**[1,2]**, R Hühne**[2]**, T Freudenberg**[2]**, A Kirchner**[2]**, L Molina-Luna**[3,4]**, C Damm**[2]**, G Van Tendeloo**[4]**, S Kaskel**[5]**, L Schultz**[2]** and B Holzapfel**[1,2,6]

[1] Karlsruhe Institute of Technology, Institute for Technical Physics, Hermann von Helmholtz Platz 1, D 76344 Eggenstein Leopoldshafen, Germany
[2] IFW Dresden, Institute for Metallic Materials, D 01171 Dresden, Germany
[3] Technische Universität Darmstadt, Department of Material and Geosciences, Alarich Weiss Strasse 2, D 64287 Darmstadt, Germany
[4] EMAT, University of Antwerp, Groenenborgerlaan 171, 2020 Antwerp, Belgium
[5] Dresden University of Technology, Dept. of Inorganic Chemistry, Mommsenstrasse 6, D 01069 Dresden, Germany
[6] TU Bergakademie Freiberg, Akademiestrasse 6, D 09599 Freiberg, Germany

E mail: manuela.erba@kit.edu

Abstract

Chemical solution deposition (CSD) is a promising way to realize REBa$_2$Cu$_3$O$_{7-x}$ (REBCO; RE = rare earth (here Y, Gd))-coated conductors with high performance in applied magnetic fields. However, the preparation process contains numerous parameters which need to be tuned to achieve high-quality films. Therefore, we investigated the growth of REBCO thin films containing nanometre-scale BaHfO$_3$ (BHO) particles as pinning centres for magnetic flux lines, with emphasis on the influence of crystallization temperature and substrate on the microstructure and superconductivity. Conductivity, microscopy and x-ray investigations show an enhanced performance of BHO nano-composites in comparison to pristine REBCO. Further, those measurements reveal the superiority of GdBCO to YBCO e.g. by inductive critical current densities, J_c, at self-field and 77 K. YBCO is outperformed by more than 1 MA cm^{-2} with J_c values of up to 5.0 MA cm^{-2} for 265 nm thick layers of GdBCO(BHO) on lanthanum aluminate. Transport in-field J_c measurements demonstrate high pinning force maxima of around 4 GN m^{-3} for YBCO(BHO) and GdBCO(BHO). However, the irreversibility fields are appreciably higher for GdBCO. The critical temperature was not significantly reduced upon BHO addition to both YBCO and GdBCO, indicating a low tendency for Hf diffusion into the REBCO matrix. Angular-dependent J_c measurements show a reduction of the anisotropy in the same order of magnitude for both REBCO compounds. Theoretical models suggest that more than one sort of pinning centre is active in all CSD films.

Keywords: REBCO, BHO, nanocomposite, chemical solution deposition, pinning

1. Introduction

In recent years, the industrial interest in bringing YBa$_2$Cu$_3$O$_{7-x}$ (YBCO) and its rare-earth analogues into applications such as high-field magnets, cables, motors, transformers and fault current limiters has increased considerably. However, there is still a significant need for improvements of production processes and resulting material properties. In particular, REBCO (RE = rare-earth elements like Y, Gd) needs to be prepared at lowest possible costs in order to be competitive with materials being used so far for such devices. Additionally, the preparation process should be

reproducible and simple, but yet, allow for highest performances. All these requirements might be solved with the TFA-MOD process, which is based on metal-organic decomposition (MOD) of trifluoroacetate (TFA) precursors deposited on a substrate. This method is a chemical solution deposition (CSD) technique and was developed by Gupta *et al* [1] in 1988 based on the preliminary work of Mankievich *et al* [2]. Several modifications of this process have been reported to date [3 7] to further improve the material or simplify the processes. However, despite all these efforts, there is still room for improvement regarding critical current densities J_c, especially in high applied magnetic fields. This is not a big surprise, as numerous parameters can be tuned in this approach to affect not only the final properties but also the expense. A key aspect of research is the reduction of processing time to limit the costs, which in general requires precursor modifications. But a reduction of energy input at similar production times can also lower costs. This makes it necessary to precisely determine phase formation temperatures for different *RE*BCO compounds in order to choose the optimal system to maximize performance at minimal costs.

Furthermore, the enhancement of in-field properties is of great interest. For this purpose, secondary phases were included by several groups to form non-superconducting nano-sized precipitates in the biaxially textured YBCO matrix which are able to immobilize flux lines [8 10]. Such vortex pinning is essential to prevent dissipation in the mixed state and consequently achieve high critical currents. The best known and investigated phase is BaZrO$_3$ (BZO) [11 13] as it precipitates well with a low tendency for substitution on *RE*BCO sites. Also tantalates [14], stannates [15, 16], double perovskites [17 20], and pinning based on non-stoichiometric *RE*BCO [7, 21 23] have been shown to raise pinning force densities, not only for *RE*BCO derived by CSD but also for cuprates grown by other methods like metal-organic chemical vapour deposition (MOCVD) or pulsed laser deposition (PLD). First and continuative investigations on other group IV and XIV compounds which form perovskite structures similar to BZO were carried out using PLD and reported in [24, 25]. The improvements demonstrated for the addition of BaHfO$_3$ (BHO) were also transferred to the CSD route with promising results for solutions of metal-organic salts in propionic acid [26]. Based on these studies, we started a broad investigation on a different solution type with improved long-term stability and reproducibility to examine the interplay among the composition of the precursor solution, the substrate, the phase formation temperature, and the final film properties. Special attention was drawn to a comparison between pristine and BHO-containing *RE*BCO films, where *RE* was chosen to be yttrium or gadolinium. In particular, the first good TFA-MOD results on pristine GdBCO by Iguchi *et al* (2.9 MA cm^{-2} for 180 nm thick films) [27] and by Jin *et al* (1.8 MA cm^{-2}) [28] were promising for further J_c increase by BHO addition. That this is indeed the case will be demonstrated in the following.

2. Synthesis and characterization

The general principle of CSD processing based on the TFA-MOD route consists of three steps: (1) preparation of a precursor solution, (2) coating on a substrate, and (3) thermal treatment. For recent investigations, four solutions were needed in total: two pristine *RE*BCO solutions, YBCO and GdBCO, which were prepared in the same way as our 'standard' solutions and two solutions of YBCO and GdBCO with hafnium additions [29]. For Hf-containing solutions, an amount of hafnium(IV)-2, 4-pentanedionate (97+%, *Alfa Aesar*) corresponding to 12 mol% in relation to *RE* is added to a batch solution, which contains an equivalent amount of Ba^{2+} to prevent a sub-stoichiometry of the final *RE*BCO phase.

For spin-coating, a very simple lab-scaled tool for depositing precursor solutions onto square-shaped substrates of small size, a substrate is mounted on a rotatable plate and covered with the solution. Through the acceleration and rotation of the plate, excessive liquid is removed from the substrate and only a thin gel-like film remains. The solutions were spin-coated on $10 \times 10 \times 1$ mm^3 (100) oriented LaAlO$_3$ (LAO) and SrTiO$_3$ (STO) single crystal substrates at a rotation speed of 6000 rpm for 30 s, leading to a final layer thickness of (265 ± 25) nm. During thermal treatment, the pyrolysis and the crystallization/oxygenation were carried out separately, which allows the pyrolysis of up to six samples in one step and enables the investigation of crystallization individually for each sample through the application of different growth temperatures (T_{growth}). A more detailed description of our standard sample preparation has been reported before in [29].

The structural quality of the samples was determined by x-ray diffraction (XRD; PW3020, *Philips*, with Co-K$_\alpha$ radiation) and scanning electron microscopy (SEM; XL20, *Philips*, secondary electrons detector, 20 kV acceleration voltage). The layer thickness was determined by atomic force microscopy (AFM; Dimension 3100, *Digital Instruments*, with silicon tips by *Nanosensors*) on the transport bridges, and by cross sectional SEM analysis after a focused ion beam (FIB) cut (Helios NanoLab 600i, *FEI*, in-lense detector, 3 kV acceleration voltage). Further structural information was attained through nano-diffraction carried out by transmission electron microscopy (TEM; Tecnai T20, *FEI*, LaB$_6$-cathode, 200 kV acceleration voltage) on FIB-cut lamellae (thickness <100 nm). Interpretation of the diffraction patterns was done by ELDISCA software [30]. A micro-pillar was prepared for on-axis electron tomography using an FEI Nova Nanolab 200 DualBeam SEM-FIB system. The pillar form of the sample allows for a full tilt range and avoids missing wedge artefacts during tomographic reconstruction [31, 32]. For electron tomography, the micro-pillar was mounted on a dedicated Fischione 2050 on-axis rotation tomography holder allowing a 360° image acquisition. A series of 2D High-Angle Annular Dark-Field (HAADF) scanning transmission electron microscopy (STEM) images was recorded over a tilt range of 180°
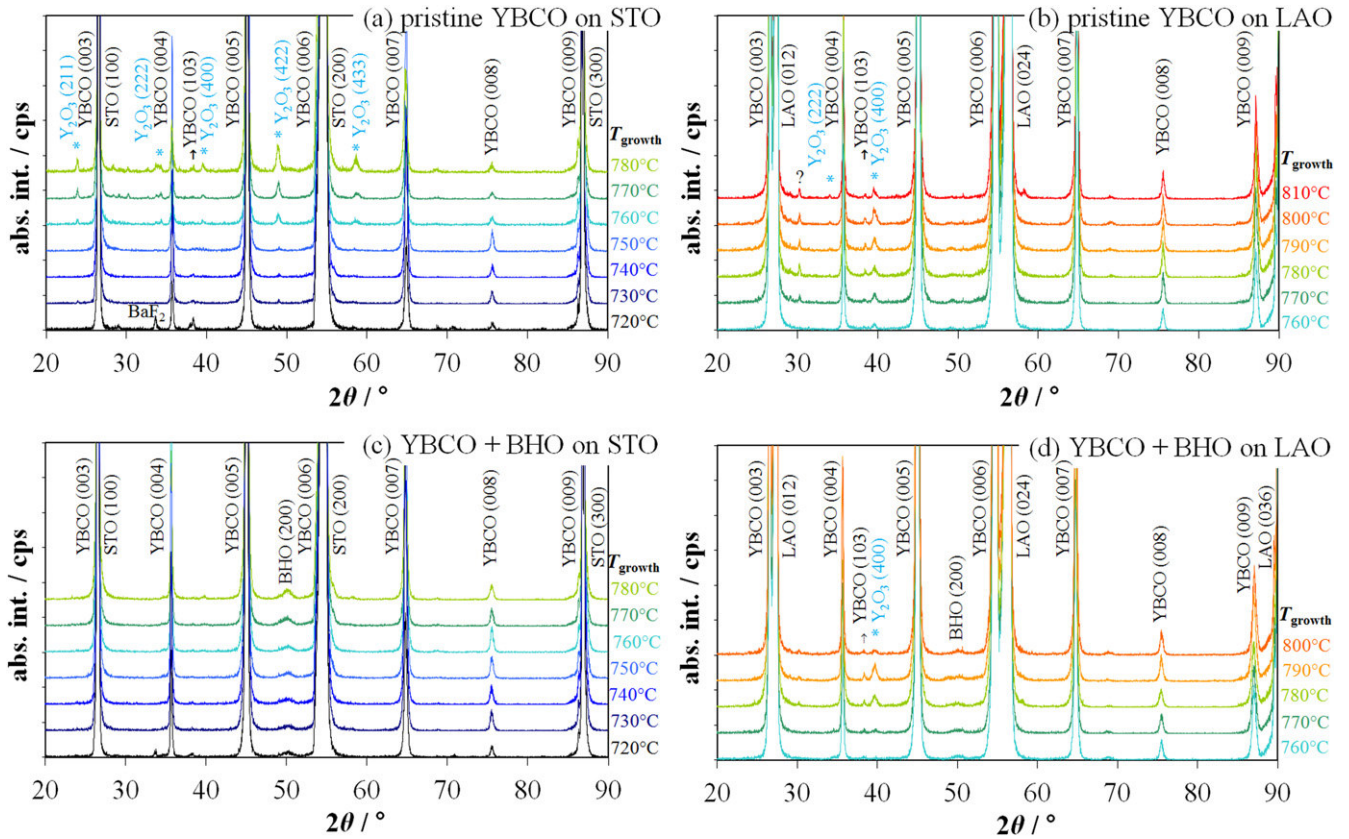
Figure 1. XRD Θ 2Θ scans of temperature series of pristine YBCO on STO (a) and LAO (b), as well as YBCO + BHO on STO (c) and LAO (d). Single data sets were shifted for clarity.

with $2°$ tilt increments using a FEG-TECNAI (Scanning) transmission electron microscope operating at $200\,kV$. The alignment of the micrographs was done using the SIRT [33] cross-correlation algorithm for the 3D reconstruction. Visualization was done using AMIRA software [34].

To scan the superconducting quality of the samples, all films were routinely analysed by inductive techniques, that is, the self-field critical current density $J_c^{sf}(77K)$ (Cryoscan, *Theva*) and critical temperature T_c. The inductive J_c values are derived from the third harmonic of the self-induction signal of a small coil directly above the film, which is immersed in liquid nitrogen. The calibration of the Cryoscan was done with a standard PLD-YBCO sample of 300 nm thickness and corresponds to the usual $1\,\mu V\,cm^{-1}$ criterion of transport J_c measurements.

For electrical transport measurements, $50\,\mu m$ wide bridges were prepared by wet-chemical etching after photolithographic masking. Photolithography is a process to generate precisely shaped structures in laminar thin films through the application of a photosensitive resist and subsequent selective removal of non-exposed parts of this resist. With that, a protective mask is generated on the film surface, allowing for physical or chemical etching of the non-protected layer. The transport measurements were performed in four-probe configuration (i.e. $J_c(B,77K)$, $J_c(\Theta)$ at several fields and temperatures, and $R(B, T)$) on selected samples. The angle Θ is spanned between the field B and the YBCO lattice

parameter c with the rotation axis along the sample bridge and therefore along the applied current (maximum Lorentz force measurements). Irreversibility fields B_{irr} were estimated with a J_c criterion of $100\,A\,cm^{-1}$. The resistive in-field measurements were carried out up to 9 Tesla on a physical properties measurement system (PPMS; *Quantum Design*, $1\,\mu V$ criterion).

3. Results and discussion

Using the example of YBCO, XRD data in figure 1 demonstrate the growth of $(00l)$ oriented *RE*BCO throughout the entire range of investigated growth temperatures. Also, the formation of BHO is evidenced within Hf-containing YBCO (figures 1(c) and (d)) through the occurrence of a broad (200) reflection belonging to a textured fraction of the perovskite phase. Yet, the textural quality of *RE*BCO and formation of secondary phases is strongly dependent on the system and the applied growth temperature, as will be discussed later.

3.1. Dependence of superconducting properties on the growth temperature

3.1.1. Critical current densities in self-field. As figure 2(a) illustrates, the self-field critical current densities at $77\,K$ ($J_c^{sf,77}$) in dependence on T_{growth} suggest an optimal growth of
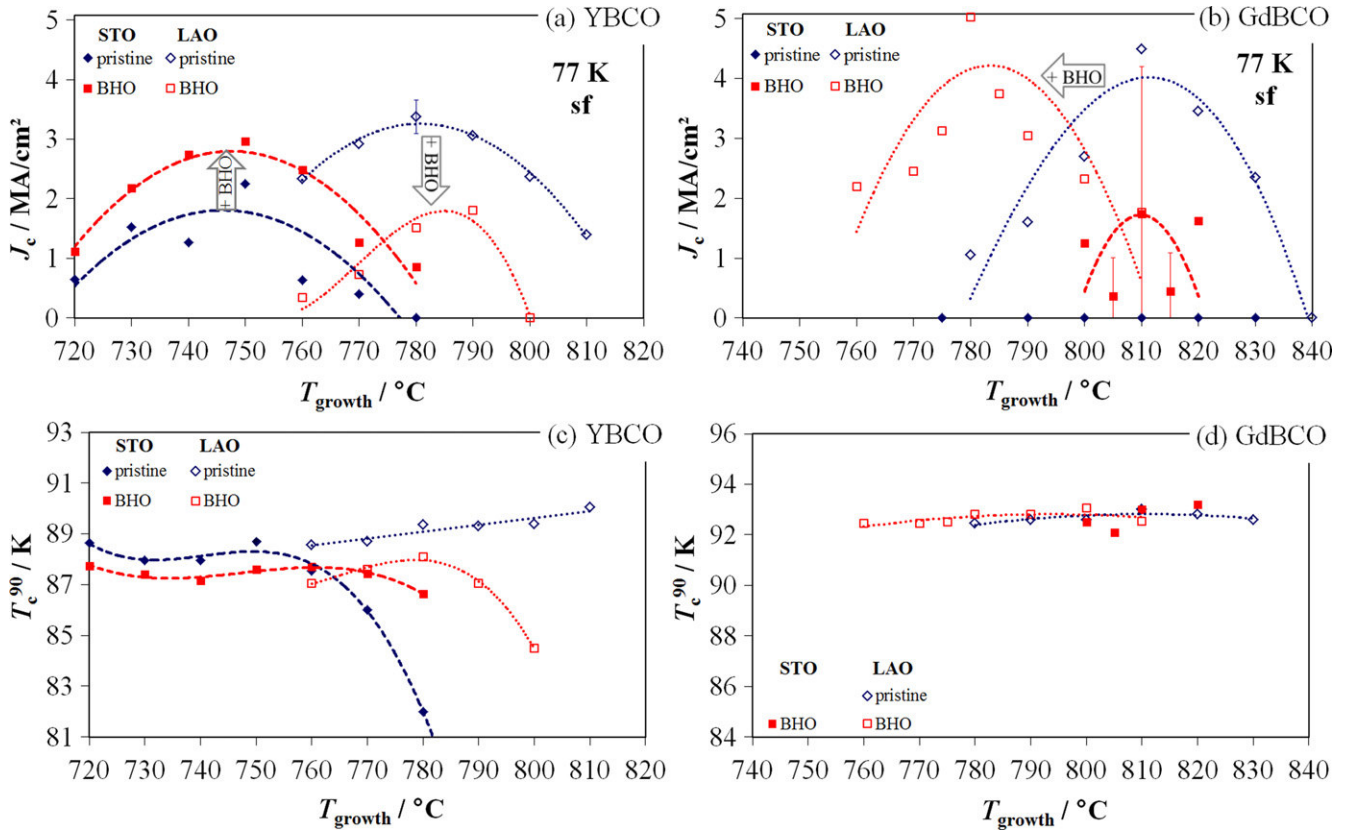
Figure 2. Top: inductive J_c versus T_{growth}; bottom: inductive T_c^{90} versus T_{growth}; (a), (c) YBCO, (b), (d) GdBCO. Filled symbols show *RE*BCO on STO, open symbols on LAO. Blue curves stand for pristine, red for BHO containing *RE*BCO. Dotted lines act as guide for the eye.

pristine YBCO on LAO at 780 °C and, therefore, at a temperature about 30 °C higher than on STO. But optimized $J_c^{sf,77}$ values for YBCO/STO are with $(2.0 \pm 0.3)\,\mathrm{MA\,cm}^{-2}$ more than $1\,\mathrm{MA\,cm}^{-2}$ smaller compared to the values for YBCO/LAO $[(3.5 \pm 0.2)\,\mathrm{MA\,cm}^{-2}]$.

The effect of BHO incorporation on $J_c(T_{growth})$ depends on the substrate. On STO, it leads to a significant increase of $J_c^{sf,77}$ (to about $3\,\mathrm{MA\,cm}^{-2}$), whereas a significant decrease was repeatedly observed on LAO, resulting in values of less than $2\,\mathrm{MA\,cm}^{-2}$. The optimal growth temperatures stayed constant in both cases.

For GdBCO, no superconductivity was found at 77 K on STO despite the investigation of a broad range of growth temperatures from 775 °C to 830 °C. In contrast, such films show high performance at similar conditions on LAO with $4.5\,\mathrm{MA\,cm}^{-2}$ at 810 °C, which demonstrates that GdBCO is stable under those growth conditions (figure 2(b)). Similar observations were made by Cao *et al* for very thin films grown by PLD [35]. Their experiments showed a severely decreased and strongly thickness-dependent T_c for GdBCO on STO. They also showed a slight deterioration for YBCO on STO, while both *RE*BCO phases were achieved with adequately high and narrow transitions on other types of substrates. Kaneko *et al* [36] suggested a low water partial pressure for high-quality GdBCO films on STO $(2.3\,\mathrm{MA\,cm}^{-2}$ for 200 nm films grown at around 800 °C) in order to suppress *a*-axis growth. Indeed, we observe a weak

a-axis but also the (103) component as well as significantly reduced (00*l*) intensities in general. Thus, the overall microstructure appears disturbed on this kind of substrate.

The behaviour of Hf-containing GdBCO solutions is very different from YBCO and is again dependent on the substrate. Samples grown on LAO show $J_c^{sf,77}$ values up to $5.0\,\mathrm{MA\,cm}^{-2}$ at 780 °C. Most importantly, lower processing temperatures are possible for the GdBCO nano-composites on LAO in comparison to pristine films. Good nano-composites could be obtained on STO as well. However, the reproducibility of $J_c^{sf,77}(T_{growth})$ is extremely poor, and the temperature window is very narrow and shifted to higher temperatures compared to GdBCO(BHO)/LAO. In summary, all of them — the *RE* element, the substrate, and the BHO content — have a strong influence on the optimal growth temperature.

3.1.2. Critical temperature. In contrast to the bell-shaped $J_c^{sf,77}(T_{growth})$ curves, T_c, and in particular T_c^{90} (defined at 90% induced voltage just above T_c), show a rather steady behaviour over the annealing temperature (figure 2, bottom). For only two YBCO systems (pristine on STO and +BHO on LAO), we observed inductive T_c^{90} to drop significantly at higher temperatures, resembling J_c. At temperatures below the maximum of $J_c^{sf,77}$, such drops do generally not occur. T_c^{90} decreases very slowly or remains nearly constant down to very low growth temperatures of 720 °C for YBCO. Even the transition widths
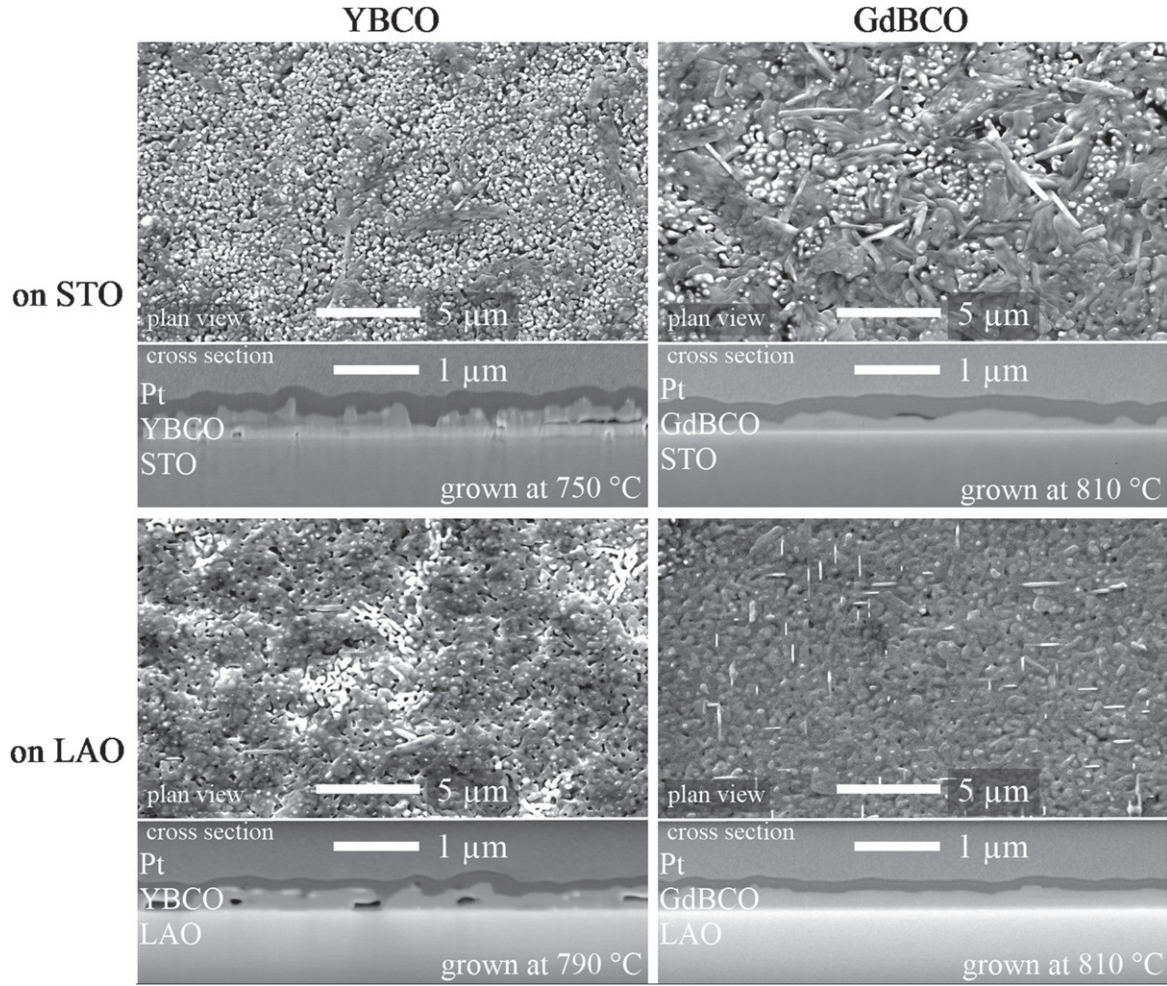
Figure 3. SEM plan view and cross sectional images for T_{growth} optimized pristine REBCO samples.

($\Delta T_{\text{c}} = T_{\text{c}}^{90} - T_{\text{c}}^{10}$) increase only slightly to the edges of the investigated temperature ranges (not shown). Accordingly, it might be concluded that the microstructure rather than T_{c} causes the curve progression of $J_{\text{c}}^{\text{sf},77}(T_{\text{growth}})$.

A comparison of the T_{c}^{90} values for different compositions shows a slight reduction after Hf addition in YBCO, as reported in the literature for BZO and BHO in PLD-YBCO on STO [13, 24]. In [24], this effect was observed to increase with the pulse number on the Hf target and therefore with the amount of secondary-phase precipitates. But due to the fact that a pure Hf metal target was used and the Ba was not counterbalanced, this effect might also be attributed to the non-stoichiometry of YBCO to a certain extent. In [13], the T_{c} reduction by Zr (Ba-compensated) did not exceed 3 K. However, in the present case, the T_{c} reduction was very low on STO ($\sim$1 K, Ba-compensated), but increased significantly when the Ba loss was not compensated (not shown)   in agreement with [20].

Such a significant reduction of 1 K and more has not been observed for GdBCO/BHO nano-composites on LAO. In contrast, Hf addition is beneficial for GdBCO on STO to achieve superconducting samples at 77 K   due to the need to overcome decomposition issues at the substrate interface, as

will be demonstrated below. Furthermore, T_{c} values were also determined resistively in a PPMS device for roughly every other sample and did not show any significant T_{c} depression after Hf additions in both YBCO and GdBCO (not shown). This supports a generally very low tendency for Hf diffusion into the REBCO lattices.

3.2. Microstructural properties

3.2.1. Pristine REBCO. Structural investigations by SEM for films representing highest inductive J_{c} within the pristine REBCO systems are displayed in figure 3 in the form of plan-view and cross-sectional images (YBCO left, GdBCO right). A look at the plan view images shows a low degree of density and homogeneity for the two YBCO samples. On STO, the surface appears very grainy, and on LAO, some buckling occurs. Better results are found for GdBCO/LAO with very compact layers and smooth surfaces, while the growth on STO is strongly disturbed by misorientations and an inhomogeneous grain size distribution.

The cross sections of the two pristine YBCO samples in figures 3 and 4 reveal a central issue of CSD films   the formation of subsurface pores and deep holes, which might
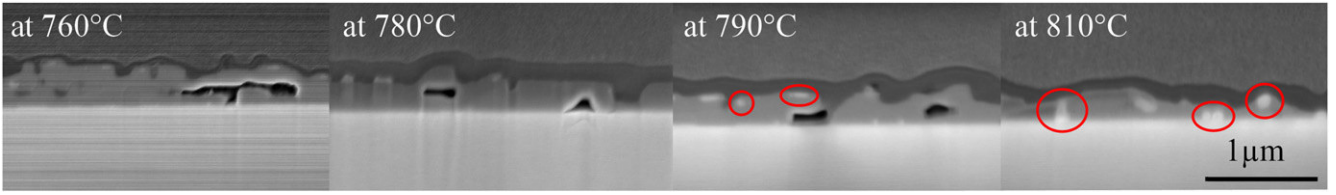
Figure 4. Cross sectional SEM of a temperature series of pristine YBCO on LAO. The circles mark large precipitates of a second phase.
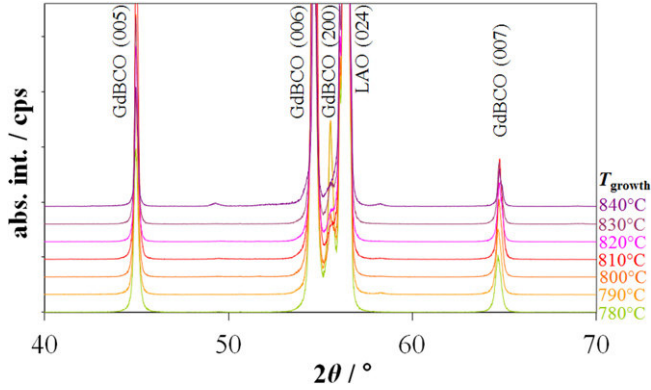
Figure 5. Detail of XRD Θ 2Θ scans of a temperature series of pristine GdBCO on LAO demonstrating significant *a* axis growth at lower temperatures. Single data sets were shifted for clarity.

block the current and lead to a reduced J_c. In YBCO, this problem becomes more severe with lower crystallization temperatures (figure 4). However, it is almost negligible for pristine GdBCO/LAO in the investigated temperature window. As T_c remains rather constant in both YBCO and GdBCO over a large growth temperature range, this pore formation can be considered one of the main reasons for the drop of J_c in YBCO at temperatures lower than the optimum. In GdBCO/LAO, on the other hand, a decrease of T_{growth} of only 10 °C below the optimal temperature leads to a significant *a*-axis fraction, which increases dramatically with decreasing temperature. Thus, the formation of misorientations might be mainly responsible for the decrease of J_c in GdBCO/LAO at lower growth temperatures. Even at optimized temperature, a few needle-shaped grains are visible in the plan-view SEM images in GdBCO/LAO samples (figure 3, bottom right), which are commonly attributed to *a*-axis orientation if aligned parallel to the substrate (100) orientations. Those *a*-axis grains are also clearly evidenced by XRD investigations in figure 5.

At growth temperatures higher than those for the J_c optimum, pores are further reduced, but secondary phases start precipitating in a large scale, as becomes visible in the form of white spots in the SEM cross sections in figure 4, marked by red circles. For YBCO/STO, the according x-ray reflections become significant at $T_{growth} > 760$ °C (figure 1(a)). XRD shows secondary phases in YBCO/LAO at $T_{growth} > 760$ °C, too, but the prominent reflections occur at different 2Θ positions compared to STO (figure 1(b)). Most of the prominent reflections on both substrates can be indexed quite well by Y_2O_3. However, the ratio of the intensities on STO for Y_2O_3 (211) at 2Θ ∼ 23.9° and (422) at 2Θ ∼ 48.9°

is opposite to the expected. Possible reasons are incorporation of foreign ions or disorder in general. Finally, nano-diffraction on such particles spotted within TEM lamellae clearly proved them to be Y_2O_3 on both types of substrates with preferential orientations on LAO and rather random development on STO, although no direct attachment to the substrate interface was observed for the particles found in the investigated lamellae.

At highest growth temperatures, those particles can grow as large as half the layer thickness (figure 4) and, thus, act as current blockers, similarly to pores. In the considered temperature range it was not possible to find YBCO free of both pores and large particles. A very simple tool to reduce porosity and surface inhomogeneities significantly are solution modifications with complexing agents, as we demonstrated through the addition of acetyle acetone [29].

EDX line scans on the same TEM lamellae revealed another important fact: At highest temperatures, titanium is clearly found within the YBCO matrix throughout the entire layer, but not in yttria particles. Thus, STO is obviously gradually losing its chemical inertness at high annealing temperatures, leading to Ti diffusion into the *RE*BCO lattice and thereby to severely reduced T_c. Consequently, this must also lead to a deterioration of the substrate interface, manifesting in the present loss of textural quality, which becomes even more severe in the case of GdBCO due to the need for higher T_{growth}. On LAO, no significant indications for substrate decomposition were observed.

3.2.2. Hf-containing REBCO. The addition of Hf leads to a strong dependence of pore formation on the growth temperature for both YBCO and GdBCO. Large pores and deep grooves occur at lower temperatures similarly to pristine YBCO and are reduced with increasing T_{growth}. However, while in YBCO nano-composites it is mainly the pore size that is affected by temperature, GdBCO nano-composite films also reduce the absolute number of pores until complete vanishing, which leads to very smooth and homogeneous films at higher temperatures (figure 6).

Temperatures above the J_c optimum lead to the growth of secondary-phase particles in nano-composite films, too, but not to the same extent as in pristine *RE*BCO phases. On STO in particular, XRD reflections caused by secondary phases become visible only at the highest temperature of 780 °C and only with a very low signal/noise ratio (figure 1(c)). On LAO, both pristine and BHO-containing YBCO (figures 1(b) and (d)) show a gradually increasing intensity of Y_2O_3 reflections up to 800 °C and 790 °C, respectively.
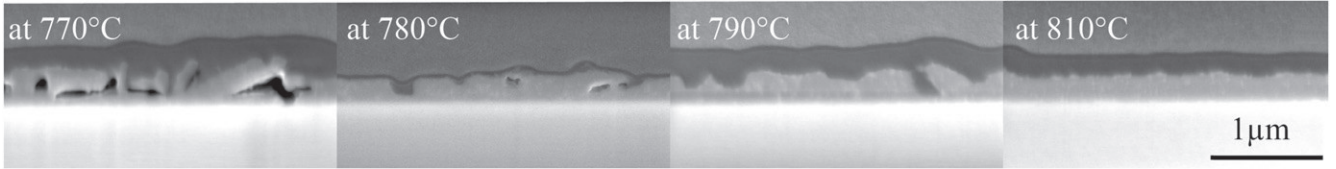
Figure 6. Cross sectional SEM of a temperature series of GdBCO + BHO on LAO.
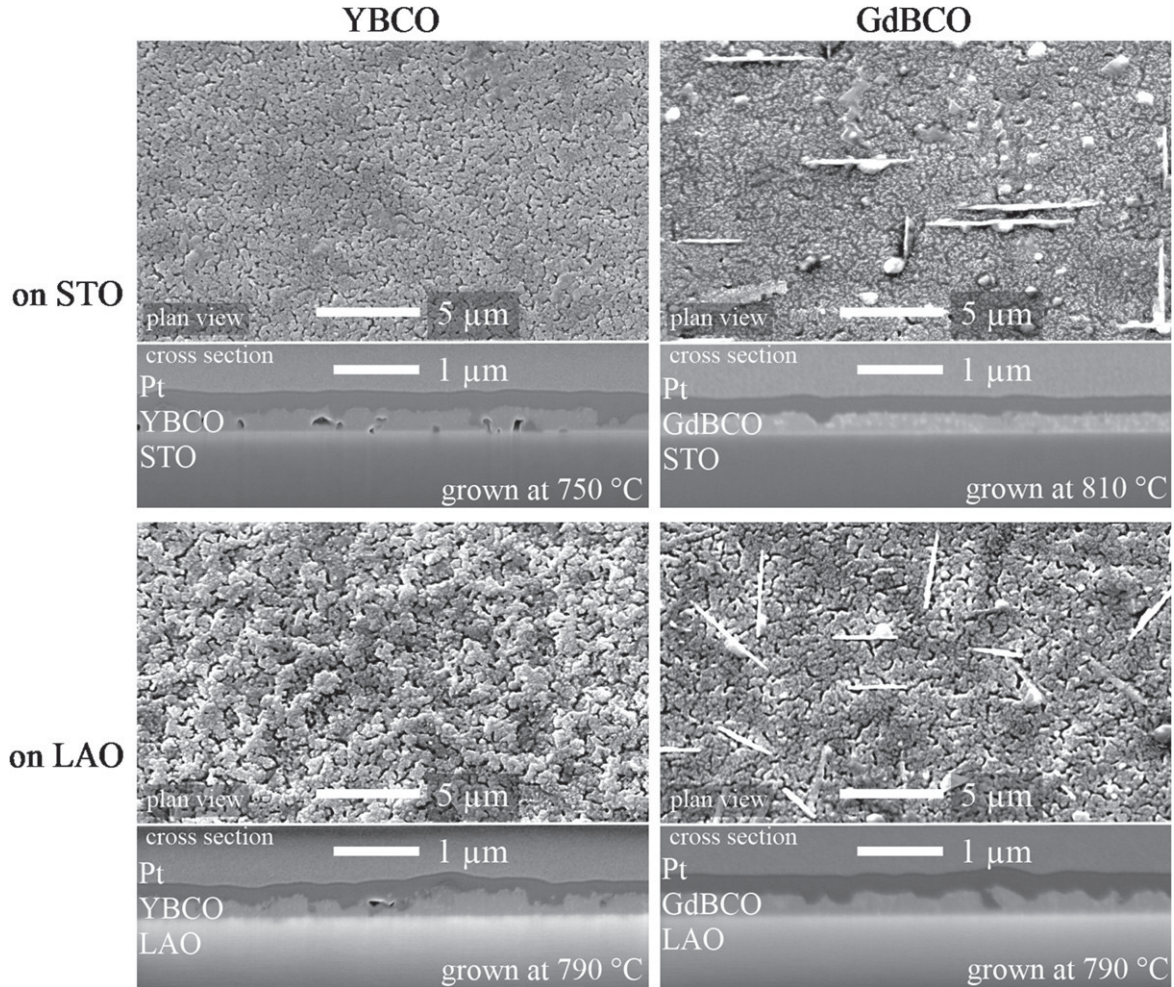
Figure 7. SEM plan view and cross sectional images for T_{growth} optimized BHO containing REBCO samples.

The significant and reproducible deterioration of $J_c^{\text{sf,77}}$ after Hf additions in YBCO/LAO at all investigated temperatures originates from a disturbed growth on this substrate (figure 7 bottom left). Even when highest J_c values are obtained at 790 °C, the interconnection between the grains is apparently very loose, and in XRD Θ 2Θ scans a weak YBCO (103) fraction is observed for the entire temperature range (figure 1(d)). At the lowest investigated temperature (760 °C), several large needle-shaped grains of more than 5 μm length occur, disturbing an otherwise well-grown c-axis texture. Those grains are randomly oriented with respect to specific substrate orientations and, thus, cannot be attributed to a-axis texture by XRD, either.

This loss of well-aligned c-axis growth on LAO might be due to the large lattice misfit between BHO and the substrate

of approximately −10%, while it is only about −6.8% on STO. Consequently, the BHO particles, which form prior to the YBCO matrix and settle at the substrate interface, might have a larger fraction of random orientation on LAO, while they grow preferentially with cube-on-cube texture on STO [37]. This is evidenced in XRD Θ 2Θ scans (figure 1, bottom), where the (200) BHO reflection, representing mainly the cube-on-cube fraction, is clearly visible on STO substrates but much weaker and more diffuse on LAO. Therefore, this oriented fraction must represent the interfacial particles to a large extent. As a consequence, the formation of randomly oriented BHO grains at the interface of LAO might disturb the nucleation of YBCO, leading to reduced J_c values for BHO-containing films on this substrate. For GdBCO nano-composites on LAO, random growth is observed, too, but is
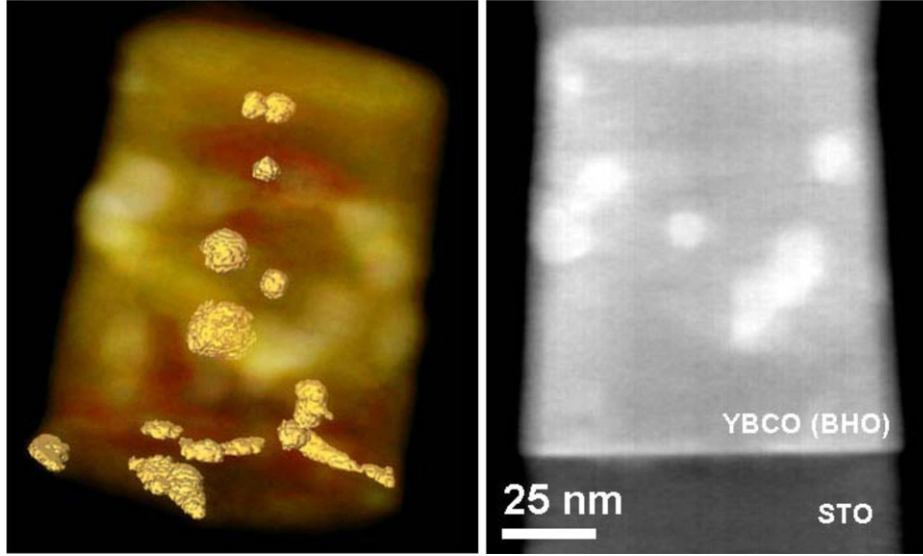
Figure 8. Electron tomography: 3D visualization of BHO nano particles on STO grown at 770 °C (left) and *xy* orthoslice through the 3D reconstruction (right).
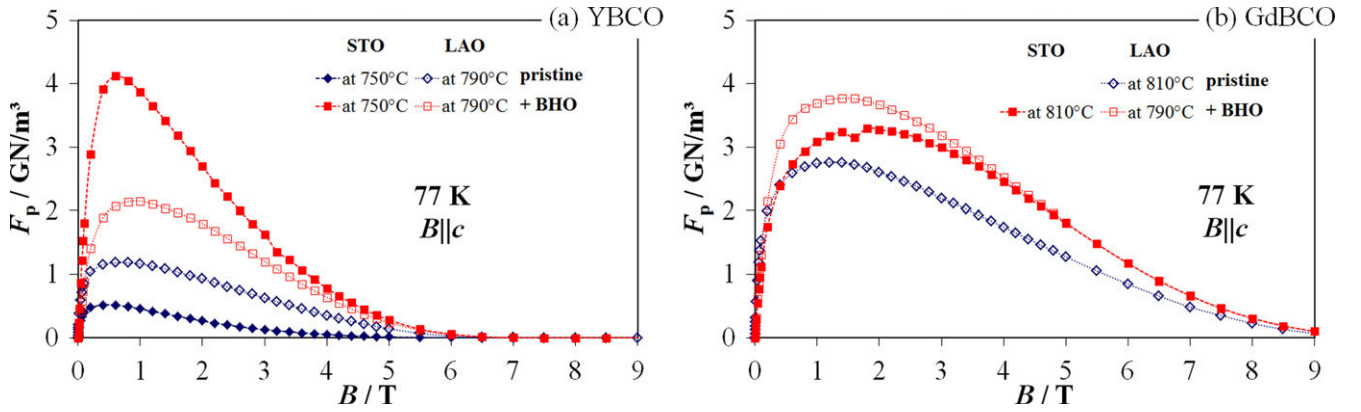
Figure 9. Pinning force densities $F_p(B)$; (a) YBCO, (b) GdBCO. The samples selected achieved highest F_p^{max} in their series.

rather focused on a few needle-shaped grains (figure 7) with a sharp *c*-axis texture in between, allowing for higher inductive J_c values. Comparable to YBCO + BHO on LAO, those randomly aligned grains could not be correlated to an *a*-axis fraction in an x-ray diffraction pattern.

In fact, a strongly attractive interaction between BHO particles and the substrate interface has been demonstrated by electron tomography 3D visualization (figure 8) for YBCO + BHO on STO, where a few spherical particles were recorded in the matrix (average size 15 nm), while the particles at the interface are rather flat and occupy the interface with a very high areal density. Thus, on STO, the presence of cube-on-cube oriented particles at the interface also seems to significantly preserve the texture information of the substrate at temperatures above 750 °C and set a barrier against Ti diffusion into the layer. Consequently, T_c values are maintained up to higher growth temperatures and the layers show less random growth, but a few *a*-axis grains in GdBCO layers (figure 7, top). However, the high growth temperatures required for GdBCO nano-composites explain the low reproducibility of high-performance samples.

3.3. In-field properties

Transport measurements on structured bridges were performed in magnetic fields up to 9 T for samples showing good superconducting properties by inductive methods.

3.3.1. Pinning force densities. For some of the investigated systems, the highest F_p^{max} values were found at slightly higher annealing temperatures than highest T_c and self-field J_c, which seems to suggest that an increased in-field performance needs slightly higher T_{growth} than the self-field performance. This is summarized in figure 9 for $T = 77$ K.

Pristine YBCO shows relatively poor pinning behaviour at 77 K on both substrates. F_p^{max} on LAO was 1.2 GN m^{-3} at fields as low as 0.5 Tesla and irreversibility fields B_{irr} below 6.5 T. The performance on STO is even worse: only 0.5 GN m^{-3} at 0.4 T. As the inductive measurements at self-field have already suggested, an inversion of the trend after Hf addition can be found on the two substrates: YBCO + BHO on STO exceeds LAO-grown YBCO nano-composites by nearly 100%. While STO leads to F_p^{max} of 4.1 GN m^{-3} at
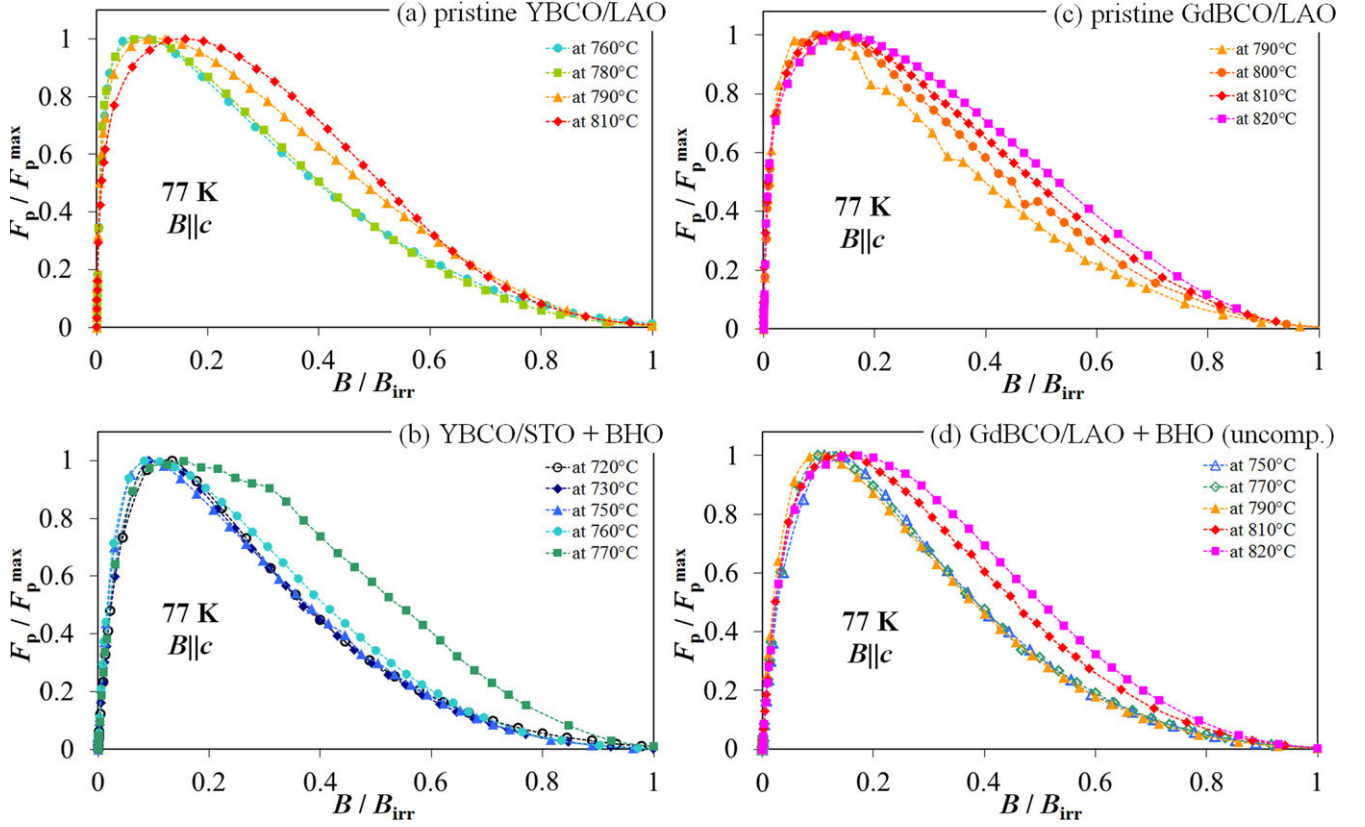
Figure 10. Normalized pinning forces F_p/F_p^{max} versus normalized fields B/B_{irr} for four different T_{growth} series: (a) pristine YBCO on LAO, (b) YBCO + BHO on STO, (c) pristine GdBCO on LAO and (d) GdBCO + uncompensated BHO on LAO. The curves show a typical shift of the pinning force maximum towards higher normalized fields for increasing T_{growth}.

0.6 T, LAO comes up to only 2.1 GN m^{-3} at 0.9 T. Compared to pristine films on LAO, F_p^{max} is enhanced through BHO addition despite the deterioration of self-field J_c values.

In contrast, GdBCO shows very good pinning on LAO even without secondary phase additions: more than 2.7 GN m^{-3} at 1.2 T and a very flat decrease to higher fields with B_{irr} beyond 9 T. T_c and other intrinsic effects contribute to the enhancement compared to YBCO. But a higher density of pinning centres induced by the larger lattice misfit to the substrate might also contribute. For clarity, further investigations of the local defect structure are required. Hf additions lead to further enhancement of F_p^{max} in GdBCO/LAO with $F_p^{max} = 3.8$ GN m^{-3} at 1.2 T. Within the limits of error, this value is roughly the same as F_p^{max} of YBCO + BHO on STO, but in higher fields GdBCO + BHO exceeds all YBCO samples considerably. Even more remarkable is the enhancement from pristine GdBCO on STO, which is not superconducting at 77 K, to GdBCO + BHO on STO with 3.3 GN m^{-3} at 1.8 T.

3.3.2. T_{growth} dependence of the pinning force density.
Figure 10 shows growth temperature series of the normalized pinning forces $f_p = F_p/F_p^{max}$ as a function of the normalized magnetic field $b = B/B_{irr}$: pristine YBCO and GdBCO on LAO ((a) and (c)) and YBCO + BHO on STO (b). Also, a series of GdBCO + BHO on LAO is shown (d), in which the

Ba loss through BHO formation in the GdBCO phase has not been counterbalanced in order to demonstrate that the observed effect is independent of Ba compensation as well. All these data sets are exemplary for a typical shift of the f_p maximum to higher normalized fields with increasing T_{growth} independent of RE element, substrate, and Ba compensation. Usually, f_p is fitted with the generalised Kramer model [38]

$$f_p \sim b^p (1 - b)^q, \tag{1}$$

where the parameter set (p, q) denotes a certain pinning mechanism [39]. The original models for low-T_c superconductors with negligible thermal fluctuation regions use B_{c2} for field normalization. For high-T_c superconductors, it was found empirically that B_{irr} should be used instead for normalizing the magnetic field. This is plausible since in 3D superconductors the transition to the vortex liquid region (i.e. B_{irr}) is related to B_{c2} [40], and this relation should enter the field dependence of the pinning force. However, due to the manifold of defects in CSD films — some acting as pinning centres, others as current blockers — the $f_p(b)$ curves in many cases cannot be fitted reasonably with one such simple phenomenological function. Instead, two defect contributions were found to be necessary for most of the data sets.

Figure 11 illustrates how the pinning force curves can be approximated by two species of pinning centres active at different field strengths. The ratio between the two
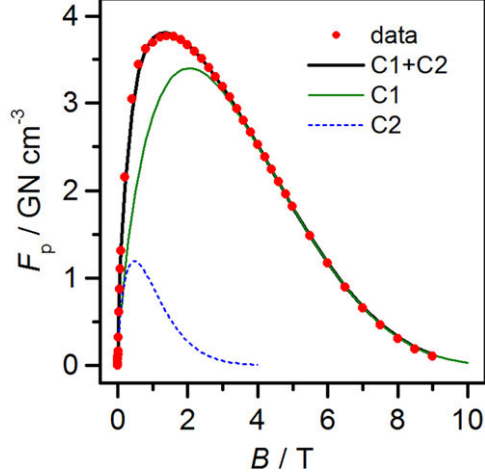
Figure 11. Fit of $F_p(B)$ data of the sample GdBCO + BHO on LAO grown at 790 °C with the sum of two contributions according to equation (1).

contributions varies monotonically with T_{growth} in favour of the contribution at higher fields (C1), leading to the observed shift of f_p^{max} to higher normalized magnetic fields. The contributions C1 and C2 have the form of equation (1). One has to keep in mind, however, that the exponents p and q have a statistical rather than a microscopic explanation here. These Kramer-like functions may be derived starting from maximum Shannon entropy considerations (leading naturally to direct summation of pinning forces expected for strong pinning) [41], or starting from microscopic considerations, e.g. [42]. This model is especially helpful if the individual contributions have maximum pinning forces at high and well-separated fields, as measured, for example, for PLD-grown YBCO/BaZrO$_3$ quasimultilayers [43]. To reduce arbitrariness of the fits, one may set either $H_{irr1} = H_{irr2}$ (chosen here with $H_{irr} = 10$ T) or $q_1 = q_2$. The resulting fit parameters for the examplary data in figure 11 are as follows: $p_1 = 1.09 \pm 0.01$, $p_2 = 0.69 \pm 0.01$, $q_1 = 3.0 \pm 0.3$, and $q_2 = 11 \pm 2$. If one is willing to correlate the fit parameters with pinning mechanisms irrespective of their statistical nature, one finds the values p in the expected range for normal core pinning at point-like defects and interfaces (0.5 1) [39]. The parameter $q_1 = 3$ is larger than the theoretical value $q = 2$ for shear breaking as the dominant pinning mechanism, but corresponds well with similar values found for other REBCO-based thin films and may be explained by large creep effects [44], collective pinning [45], or an interplay of the vortex lattice's elastic constants C_{44} and C_{66} [46]. The parameter q_2 has pure statistical meaning, as explained above.

A very common way to phenomenologically fit $J_c(B)$ is the following empirical function [47], which can be understood as a combination of the modified Kim model [48] and the generalized Kramer model:

$$J_c = J_c(0) * \left(1 + B/B_0\right)^{-\alpha} * \left(1 - B/B_{irr}\right)^q \qquad (2)$$

B_{irr} is the irreversibility field, B_0 the length of the low-field plateau related to self field and/or accommodation field, and

α ($\sim 1 - p$) and q (here fixed at 2 for simplicity) are fit parameters. Two examples of $J_c(B)$ and the according fits are shown in figure 12(a). Figures 12(b), (c) shows the T_{growth} dependence of the fit parameters α, B_{irr} and B_0 for two different GdBCO/LAO series (pristine and +BHO). Since B_0 is not positively correlated to $J_c(0)$, it is related to the accommodation field rather than the self field. B_0 decreases monotonically with T_{growth} and does not depend on the BHO content. Therefore, we conclude that it is related to extended c-axis growth defects, such as dislocations, which heal up with higher growth temperatures. This is in agreement with the observed reduction of C2, mentioned above. This dependence is correlated with the f_p^{max} shift with T_{growth} in figure 10. B_{irr}, on the other hand, depends on the BHO content and for both series seems to have an optimum. The exponent α decreases with T_{growth} (i.e. with decreasing B_0, respectively contribution C2) and BHO content (i.e. with increasing B_{irr}).

3.3.3. Angular-dependent measurements. Angular-dependent measurements of the critical current densities are displayed in figure 13 for selected samples exemplarily on LAO. The data show a reduction of the J_c anisotropy through BHO nano-particles for both REBCO phases at both fields and temperatures in a similar way. The maxima at $\Theta = 90°$ ($B\|ab$) are roughly the same for pure samples and BHO nano-composites, but usually a little bit higher without Hf addition. Besides the ab planes, BHO pinning centres cause a lifting in a wide angular range without clear peaks at $180°$ ($B\|c$) except for fields close to B_{irr}. Figure 13(c) shows scalings of the critical current density to an effective field according to [49]

$$H_{eff} = H * \varepsilon(\theta, \gamma)$$
$$\varepsilon(\theta, \gamma) = \left(\cos^2 \theta + \gamma^2 \sin^2 \theta\right)^{0.5} \qquad (3)$$

with both the expected mass anisotropy $\gamma = \gamma_m = 5$ and an effective anisotropy $\gamma = \gamma_{eff} = 1.8$ for GdBCO + BHO on LAO. Even though there is a microscopic explanation only for microstructurally clean films with small defects ($d \lesssim \xi$), this scaling is widely used as a comparative measure of the J_c anisotropy because γ is (in first approximation) B and T independent in contrast to ratios $J_c(B\|ab)/J_c(B\|c)$ or J_c^{max}/J_c^{min}. It is apparent that J_c does not scale with γ_m, due to the large density of extended defects. However, it scales fairly well with a strongly reduced effective anisotropy $\gamma_{eff} = 1.8$ in a wide angular range around $B\|c$. This effect is typical for CSD-grown films and has been observed by many groups, e.g. [50]. Even the pristine REBCO films show scaling with reduced gamma values (2.3 for GdBCO). It is interesting to note that no strong c-axis peak is visible in these CSD-grown films, although the nano-particles with mean diameters of 15 nm are much larger than ξ_c. This is in contrast to PVD-grown films, where even small nano-particles with $d \approx \xi_c$ can lead to huge c-axis peaks [51], indicating that the interplay of these isotropic, random defects with other defect species, such as ab-planar intergrowths and grain boundaries, is crucial for the J_c anisotropy in defect-engineered superconductors [52].
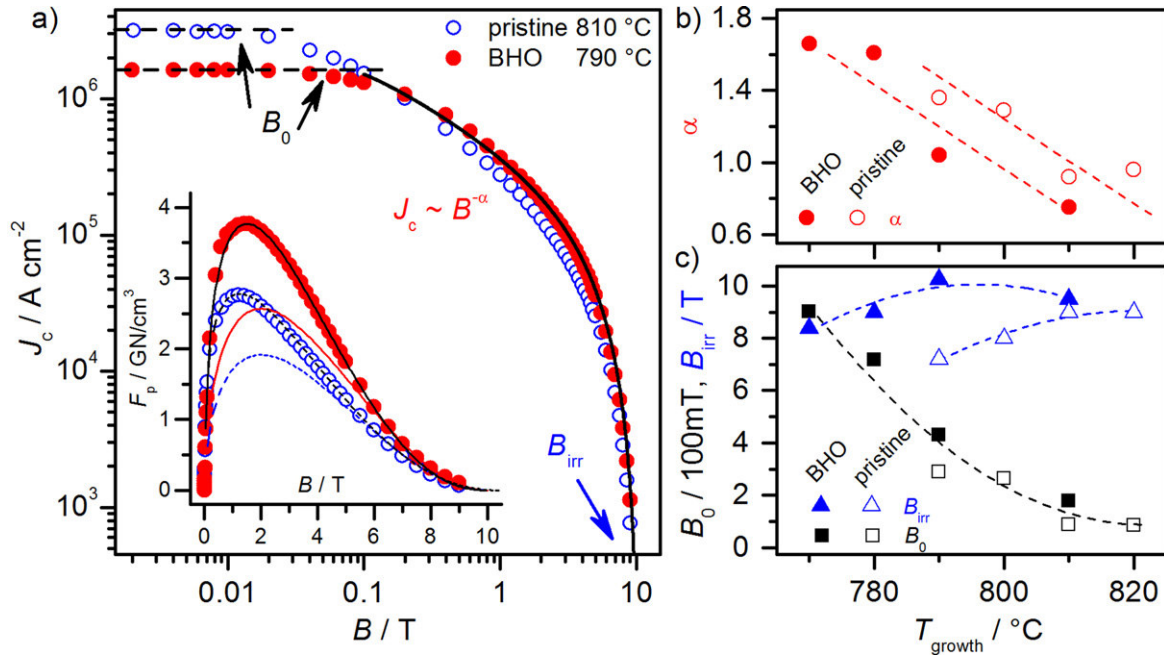
Figure 12. (a) $J_c(B)$ and $F_p(B)$ (inset) of two examples of GdBCO on LAO grown at 810 °C (pristine) and 790 °C (+BHO) illustrate the discrepancy of F_p and pure Kramer fits with $(p, q) = (0.5, 2)$ (blue and red lines). The black lines are fits according to equation (2). (b), (c) Growth temperature dependence of fit parameters for equation (2) for GdBCO/LAO with and without BHO addition.
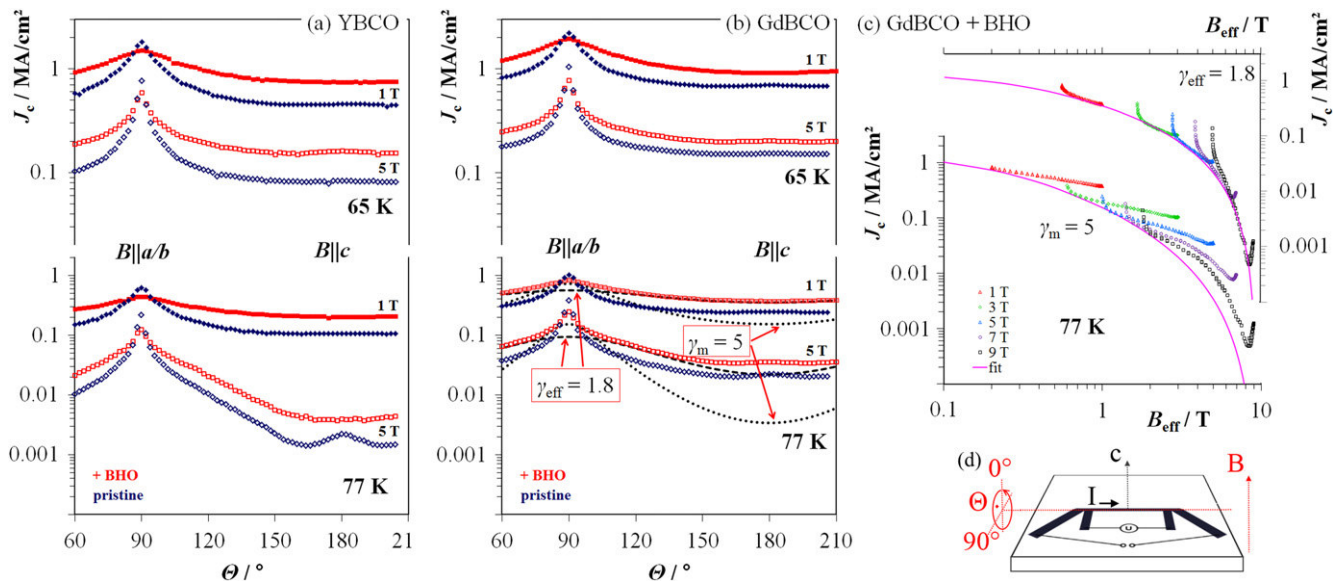
Figure 13. Angular dependence of J_c for films on LAO with (red) and without (blue) BHO addition at two fields and temperatures: (a) YBCO, (b) GdBCO (pristine GdBCO grown at 810 °C, the other films at 790 °C); (c) shows the scaling of $J_c(\Theta, B)$ to an effective field B_{eff} at 77 K for GdBCO + BHO on LAO for two different anisotropy parameters γ and the resulting fits (pink lines), from which the isotropic pinning contributions are determined and graphically demonstrated in (b) as black dashed and dotted lines. (d) shows the measurement geometry.

4. Conclusions

The comparison of two different REBCO phases of YBCO and GdBCO, pristine and with BHO nano-particles, and on two different substrates gave a thorough insight into their respective effects on microstructure and superconducting properties in terms of their dependence on the annealing temperature. Structural features were expanding pores in YBCO, and a massive augmentation of a-axis-oriented grains

in GdBCO, when the growth temperatures were reduced below the respective optima. At increased temperatures, a massive growth of secondary phase particles occurred in particular, in pristine samples. Subsurface pores, misorientations, and large secondary-phase particles (mainly yttria) were identified to be some of the main reasons for J_c reduction, as T_c remains rather unaffected by the growth temperature. A particularly interesting result was the drastically different behaviour on the commonly used substrates STO and LAO in

spite of their rather similar lattice misfits to the REBCO systems. Investigations pointed to a lack of chemical stability of STO at temperatures above 750 °C, resulting in Ti diffusion into the layer and an according decomposition of the interface, leading to T_c degradation and misoriented growth of the pristine REBCO phases. This effect was strongly reduced through the addition of Hf, which led to the formation of spherical BHO nano-particles of 15 nm size in the matrix, and rather flat-shaped particles covering large areas of the interface. Their interplay did significantly improve film properties on STO because of pinning enhancement, but also because the interfacial particles countered the decomposition of the substrate. Generally, T_c was found to be nearly unaffected by Hf addition, which indicates a very low tendency for Hf diffusion into the REBCO lattice in particular in GdBCO. The application of statistical models revealed for all CSD films that more than one pinning contribution is necessary to describe $F_p(B)$ curves with simple phenomenological functions. $J_c(B)$ curves could be fitted reasonably well above the accommodation field with a combination of the modified Kim and the generalized Kramer models. In summary, BHO nano-composites of GdBCO showed the best performance when grown on LAO at 790 810 °C, as both zero- and in-field properties were enhanced.

Acknowledgments

References

[1] Gupta A, Jagannathan R, Cooper E I, Giess E A, Landman J I and Hussey B W 1988 Superconducting oxide films with high transition temperature prepared from metal trifluoroacetate precursors *Appl. Phys. Lett.* **52** 2077 9

[2] Mankiewich P M, Scofield J H, Skocpol W J, Howard R E, Dayem A H and Good E 1987 Reproducible technique for fabrication of thin films of high transition temperature superconductors *Appl. Phys. Lett.* **51** 1753 5

[3] McIntyre P C, Cima M J, Smith J A, Hallock R B, Siegal M P and Phillips J M 1992 Effect of growth conditions on the properties and morphology of chemically derived epitaxial thin films of Ba$_2$YCu$_3$O$_{7-x}$ on (001) LaAlO$_3$ *J. Appl. Phys.* **71** 1868 77

[4] Araki T, Yamagiwa K and Hirabayashi I 2001 Fabrication of YBa$_2$Cu$_3$O$_{7-x}$ film by metalorganic deposition method using trifluoroacetates and its process conditions *Cryogenics* **41** 675 81

[5] Obradors X *et al* 2004 Chemical solution growth of superconductors: a new path towards high critical current coated conductors *Physica* C **408 410** 913 4

[6] Roma N, Morlens S, Ricart S, Zalamova K, Moreto J M, Pomar A, Puig T and Obradors X 2006 Acid anhydrides: a simple route to highly pure organometallic solutions for superconducting films *Supercond. Sci. Technol.* **19** 521 7

[7] Zhao G, Lei L, Liu X and Chen Y 2008 Effect of copper content in precursor solution on the superconducting properties of YBCO films derived from low fluorine solution *Physica* C **468** 2317 21

[8] Selinder T I, Helmersson U, Han Z, Sundgren J E, Sjöström H and Wallenberg L R 1992 Yttrium oxide inclusions in YBa$_2$Cu$_3$O$_x$ thin films: enhanced flux pinning and relation to copper oxide surface particles *Physica* C **202** 69 74

[9] Wen H H, Zhao Z X, Wang R L, Li H C and Yin B 1996 Evidence for the lattice mismatch stress field induced flux pinning in (Gd$_{1-x}$Y$_x$)Ba$_2$Cu$_3$O$_{7-\sigma}$ thin films *Physica* C **262** 81 8

[10] Haugan T, Barnes P N, Maartense I, Cobb C B, Lee E J and Sumption M 2003 Island growth of Y$_2$BaCuO$_5$ nanoparticles in (211$_{-1.5nm}$/123$_{-10nm}$) × N composite multilayer structures to enhance flux pinning of YBa$_2$Cu$_3$O$_{7-\delta}$ films *J. Mater. Res.* **18** 2618 23

[11] Alarco J A, Brorsson G, Olin H and Olsson E 1994 Early stages of growth of YBa$_2$Cu$_3$O$_{7-\delta}$ high T_c superconducting films on (001) YZrO$_2$ substrates *J. Appl. Phys.* **75** 3202 4

[12] Luo Y Y, Wu Y C, Xiong X M, Li Q Y, Gawalek W and He Z H 2000 Effects of Precursors with Fine BaZrO$_3$ Inclusions on the Growth and Microstructure of Textured YBCO *J. Supercond. Nov. Magn.* **13** 575 81

[13] MacManus Driscoll J L, Foltyn S R, Jia Q X, Wang H, Serquis A, Civale L, Maiorov B, Hawley M E, Maley M P and Peterson D E 2004 Strongly enhanced current densities in superconducting coated conductors of YBa$_2$Cu$_3$O$_{7\ x}$ + BaZrO$_3$ *Nat. Mater.* **3** 439 43

[14] Harrington S A, Durrell J H, Maiorov B, Wang H, Wimbush S C, Kursumovic A, Lee J H and MacManus Driscoll J L 2009 Self assembled, rare earth tantalate pyrochlore nanoparticles for superior flux pinning in YBa$_2$Cu$_3$O$_{7-\delta}$ films *Supercond. Sci. Technol.* **22** 022001

[15] Varanasi C V, Barnes P N, Burke J, Brunke L, Maartense I, Haugan T J, Stinzianni E A, Dunn K A and Haldar P 2006 Flux pinning enhancement in YBa$_2$Cu$_3$O$_{7-x}$ films with BaSnO$_3$ nanoparticles *Supercond. Sci. Technol.* **19** L37 41

[16] Miura M, Maiorov B, Willis J O, Kato T, Sato M, Izumi T, Shiohara Y and Civale L 2013 The effects of density and size of BaMO$_3$ (M = Zr, Nb, Sn) nanoparticles on the vortex glassy and liquid phase in (Y, Gd)Ba$_2$Cu$_3$O$_y$ coated conductors *Supercond. Sci. Technol.* **26** 035008

[17] Feldmann D M, Holesinger T G, Maiorov B, Foltyn S R, Coulter J Y and Apodaca I 2010 Improved flux pinning in YBa$_2$Cu$_3$O$_7$ with nanorods of the double perovskite Ba$_2$YNbO$_6$ *Supercond. Sci. Technol.* **23** 095004

[18] Coll M *et al* 2014 Size controlled spontaneously segregated Ba$_2$YTaO$_6$ nanoparticles in YBa$_2$Cu$_3$O$_7$ nanocomposites obtained by chemical solution deposition *Supercond. Sci. Technol.* **27** 044008

[19] Reich E, Thersleff T, Hühne R, Iida K, Schultz L and Holzapfel B 2009 Structural and pinning properties of Y$_2$Ba$_4$CuMO$_y$ (M = Nb, Zr)/YBa$_2$Cu$_3$O$_{7-\delta}$ quasi multilayers fabricated by off axis pulsed laser deposition *Supercond. Sci. Technol.* **22** 105004

[20] Ercolano G, Bianchetti M, Wimbush S C, Harrington S A, Wang H, Lee J H and MacManus Driscoll J L 2011 State of the art flux pinning in YBa$_2$Cu$_3$O$_{7-\delta}$ by the creation of highly linear, segmented nanorods of Ba$_2$(Y/Gd)(Nb/Ta)O$_6$

together with nanoparticles of $(Y/Gd)_2O_3$ and $(Y/Gd)Ba_2Cu_4O_8$ *Supercond. Sci. Technol.* **24** 095012

[21] Araki T, Niwa T, Yamada Y, Hirabayashi I, Shibata J, Ikuhara Y, Kato T and Hirayama T 2002 Growth model and the effect of CuO nanocrystallites on the properties of chemically derived epitaxial thin films of $YBa_2Cu_3O_{7-x}$ *J. Appl. Phys.* **92** 3318 25

[22] Nakaoka K, Matsuda J, Kitoh Y, Goto T, Yamada Y, Izumi T and Shiohara Y 2007 Influence of starting solution composition on superconducting properties of YBCO coated conductors by advanced TFA MOD process *Physica* C **463 465** 519 22

[23] Tada K *et al* 2008 Growth process of Ba poor YBCO film fabricated by TFA MOD process *Physica* C **468** 1554 8

[24] Hänisch J, Cai C, Stehr V, Hühne R, Lyubina J, Nenkov K, Fuchs G, Schultz L and Holzapfel B 2006 Formation and pinning properties of growth controlled nanoscale precipitates in $YBa_2Cu_3O_{7-\delta}$/transition metal quasi multilayers *Supercond. Sci. Technol.* **19** 534 40

[25] Tsuruta A, Yoshida Y, Ichino Y, Ichinose A, Matsumoto K and Awaji S 2013 Flux pinning properties at low temperatures in BaH_fO_3 doped $SmBa_2Co_3O_y$ films *IEEE Trans. Appl. Supercond.* **23** 8001104

[26] Engel S, Thersleff T, Hühne R, Schultz L and Holzapfel B 2007 Enhanced flux pinning in $YBa_2Cu_3O_7$ layers by the formation of nanosized $BaHfO_3$ precipitates using the chemical deposition method *Appl. Phys. Lett.* **90** 102505

[27] Iguchi T, Araki T, Yamada Y, Hirabayashi I and Ikuta H 2002 Fabrication of Gd Ba Cu O films by the metal organic deposition method using trifluoroacetates *Supercond. Sci. Technol.* **15** 1415 20

[28] Jin L H, Lu Y F, Yan W W, Yu Z M, Wang Y and Li C S 2011 Fabrication of $GdBa_2Cu_3O_{7-x}$ films by TFA MOD process *J. Alloys Compd.* **509** 3353 6

[29] Erbe M, Hänisch J, Freudenberg T, Kirchner A, Mönch I, Kaskel S, Schultz L and Holzapfel B 2014 Improved $REBa_2Cu_3O_{7-x}$ (RE = Y, Gd) structure and superconducting properties by acetylacetone additions in TFA MOD precursor solutions *J. Mater. Chem.* A **2** 4932 44

[30] Thomas J and Gemming T 2008 ELDISCA C# a new version of the program for identifying electron diffraction patterns, *EMC 2008 14th European Microscopy Congress 1 5 September 2008, Aachen, Germany* ed M Luysberg, K Tillmann and T Weirich (Berlin: Springer) pp 231 2

[31] Biermans E, Molina L, Batenburg K J, Bals S and Van Tendeloo G 2010 Measuring porosity at the nanoscale by quantitative electron tomography *Nano Lett.* **10** 5014 9

[32] Molina L, Tan H, Biermans E, Batenburg K J, Verbeeck J, Bals S and Tendeloo G V 2011 Barrier efficiency of sponge like $La_2Zr_2O_7$ buffer layers for YBCO coated conductors *Supercond. Sci. Technol.* **24** 065019

[33] Gilbert P 1972 Iterative methods for the three dimensional reconstruction of an object from projections *J. Theor. Biol.* **36** 105 17

[34] Stalling D, Westerhoff M and Hege H C 2005 38 amira: a highly interactive system for visual data analysis

Visualization Handbook ed C D H R Johnson (Burlington: Butterworth Heinemann) pp 749 LXXVIII

[35] Cao L X, Zegenhagen J, Sozontov E and Cardona M 2000 The effect of epitaxial strain on $RBa_2Cu_3O_7$ thin films and the perovskite substrate *Physica* C **337** 24 30

[36] Kaneko A *et al* 2004 Fabrication of $REBa_2Cu_3O_{7-y}$ film by advanced TFA MOD process *Physica* C **412 414** 926 30

[37] Thersleff T D 2011 The nanoscale characterization of functional superconducting thin films *PhD Thesis* Dresden Technische Universität

[38] Kramer E J 1973 Scaling laws for flux pinning in hard superconductors *J. Appl. Phys.* **44** 1360 70

[39] Dew Hughes D 1974 Flux pinning mechanisms in type II superconductors *Phil. Mag.* **30** 293 305

[40] Blatter G 1994 Vortices in high temperature superconductors *Rev. Mod. Phys.* **66** 1125 388

[41] Long N J 2013 A statistical mechanical model of critical currents in superconductors *J. Supercond. Nov. Magn.* 1 5

[42] Kiss T, Matsushita T and Irie F 1999 Relationship among flux depinning, irreversibility and phase transition in a disordered HTS material *Supercond. Sci. Technol.* **12** 1079 82

[43] Kiessling A, Hänisch J, Thersleff T, Reich E, Weigand M, Hühne R, Sparing M, Holzapfel B, Durrell J H and Schultz L 2011 Nanocolumns in $YBa_2Cu_3O_{7-x}$/$BaZrO_3$ quasi multilayers: formation and influence on superconducting properties *Supercond. Sci. Technol.* **24** 055018

[44] Matsushita T, Matsuda A and Yanagi K 1993 Irreversibility line and flux pinning properties in high temperature superconductors *Physica* C **213** 477 82

[45] Li P J, Wang Z H, Hu A M, Bai Z, Qiu L and Gao J 2006 The collective flux pinning force in $(Sm_{0.5}Eu_{0.5})Ba_2Cu_3O_{7-\delta}$ superconductors *Supercond. Sci. Technol.* **19** 825

[46] Sun J J, Zhao B R, Xu B, Guo S Q, Yin B, Li J W and Li L 1996 Critical current and flux pinning in c axis oriented $YBa_2Cu_3O_7$/$PrBa_2Cu_3O_7$ superlattices *Phys. Status Solidi* (a) **157** 115 20

[47] Aytug T *et al* 2005 Enhancement of flux pinning and critical currents in $YBa_2Cu_3O_{7-\delta}$ films by nanoscale iridium pretreatment of substrate surfaces *J. Appl. Phys.* **98** 114309

[48] Xu M, Shi D and Fox R F 1990 Generalized critical state model for hard superconductors *Phys. Rev.* B **42** 10773 6

[49] Blatter G, Geshkenbein V B and Larkin A I 1992 From isotropic to anisotropic superconductors: a scaling approach *Phys. Rev. Lett.* **68** 875 8

[50] Gutiérrez J *et al* 2007 Strong isotropic flux pinning in solution derived $YBa_2Cu_3O_{7-x}$ nanocomposite superconductor films *Nat. Mater.* **6** 367 73

[51] Matsui H, Ogiso H, Yamasaki H, Kumagai T, Sohma M, Yamaguchi I and Manabe T 2012 4 fold enhancement in the critical current density of $YBa_2Cu_3O_7$ films by practical ion irradiation *Appl. Phys. Lett.* **101** 232601

[52] Wimbush S C and Long N J 2012 The interpretation of the field angle dependence of the critical current in defect engineered superconductors *New J. Phys.* **14** 083017